The Empact CVT: modeling, simulation and experiments

The Empact CVT: modelling, simulation and experiments

Tim W.G.L. Klaassen,* Bram Bonsen, Koen G.O. van de Meerakker, Bas G. Vroemen, P.A. Veenhuizen, Frans E. Veldpaus and Maarten Steinbuch

Department of Mechanical Engineering,
Technische Universiteit Eindhoven,
Den Dolech 2, Eindhoven 5600 MB, The Netherlands
Fax: +31-40-246-1418
E-mail: t.w.g.l.klaassen@gmail.com
E-mail: bbonsen@gmail.com
E-mail: kvandemeerakker@gcinet.nl
E-mail: vroemen@dtinnovations.nl
E-mail: p.a.veenhuizen@tue.nl
E-mail: f.e.veldpaus@tue.nl
E-mail: m.steinbuch@tue.nl
*Corresponding author

Abstract: This paper shows the implementation of a simulation model for new electromechanically actuated metal V-belt type Continuously Variable Transmission (CVT), referred to as the Empact CVT. An analysis of the dynamics of the actuation system and of the driveline shows that the eigenfrequencies of the system depend on both the CVT ratio and the slip in the variator. An accurate variator model is required to incorporate all characteristic dynamics. The implemented variator model is an explicit formulation of a model which gives an estimation of the tension forces and compression forces in the pushbelt. The simulation model also includes slip, shifting losses based on transient variator models and friction. Simulations are compared to measurements, showing good results.

Keywords: continuously variable transmission; CVT; electromechanical actuation; power train modelling; variator modelling; dynamical analysis; simulation; experimental validation.

Reference to this paper should be made as follows: Klaassen, T.W.G.L., Bonsen, B., van de Meerakker, K.G.O., Vroemen, B.G., Veenhuizen, P.A., Veldpaus, F.E. and Steinbuch, M. (2008) 'The Empact CVT: modelling, simulation and experiments', *Int. J. Modelling, Identification and Control*, Vol. 3, No. 3, pp.286–296.

Biographical notes: Tim W.G.L. Klaassen received his MSc in Mechanical Engineering from Eindhoven University of Technology, The Netherlands, in March 2002. During his MSc project, he studied the motion control of industrial printers at Stork Digital Imaging. In April 2002, he started his PhD project, at Eindhoven University of Technology. In this project, he is working on the modelling and control of an electromechanically actuated metal V-belt CVT.

Bram Bonsen received his Mechanical Engineering at the University of Twente. He received his Masters degree in the Mechanical Automation Group of Prof.dr.ir. J.B. Jonker on a model reduction method for non-linear finite element methods. He worked two years for Cap Gemini Ernst and Young as a SAP business consultant. Within the Department of Control Systems Technology of the Eindhoven University of Technology, he is working on his PhD thesis on modelling and control of slip in the Continuously Variable Transmission (CVT).

Koen G.O. van de Meerakker (1977) graduated in Mechanical Engineering at the Eindhoven University of Technology. In 2002, he received his Masters degree in the Construction and Mechanisms group on the design of a fast DVD injection moulding press. Since then, he works as a PhD student at the same university on the design, realisation and testing of an electromechanically actuated CVT prototype.

Bas G. Vroemen received his MSc in Mechanical Engineering in 1997 from the Technische Universiteit Eindhoven. In 2001, he received his PhD at the Technische Universiteit Eindhoven, in the EcoDrive research project. The fuel-efficient hybrid drive train and its controls, designed in the project, received the Novem Energy Conversion Award and two patents were granted. Medio 2001, Bas Vroemen, Roell van Druten and Alex Serrarens have started a company

called Drive Train Innovations (DTI) to support the automotive industry with innovative ideas and fundamental knowledge regarding hybrid powertrains. He is still associated with the university as a Postdoc employee.

P.A. Veenhuizen received his MSc in Experimental Physics from the Free University of Amsterdam in 1984 and his PhD from the University of Amsterdam in 1988. After employment by SKF, (1988–1995) and van Doorne's Transmissie (1995–2002) he joined the Eindhoven University of Technology. Here, he is responsible for research on automotive power trains, focusing on V-belt type Continuously Variable Transmissions and Advanced (hybrid) power trains. In 2005, he was appointed a Professor of Vehicle Mechatronics at the HAN University in Arnhem. His professional interest is in automotive drive train systems and the implementation of academic research in the automotive industrial environment.

Frans E. Veldpaus received his MSc and a PhD from the Technische Universiteit Eindhoven (TU/e), Eindhoven, The Netherlands, in 1966 and 1973, respectively. Since 1966, he worked in the Department of Mechanical Engineering, TU/e, first in the area of structural dynamics and solid mechanics and then in the field of control of mechanical systems. His main research interests are modelling and control of automotive systems, that is, of active wheel suspensions and power trains in general and of automotive components, continuously variable transmissions in particular.

Maarten Steinbuch received his MSc and a PhD in Mechanical Engineering from Delft University of Technology in 1984 and 1989, respectively. From 1987–1999, he was with Philips Electronics. Since 1999, he has been full Professor and Head of the Control Systems Technology group within the Department of Mechanical Engineering, Eindhoven University of Technology. His research interests are modelling and control of automotive power trains and motion systems. He was an Associate Editor of the *IEEE Transactions on Control Systems Technology, IFAC Control Engineering Practice and IEEE Control Systems Magazine.* He is currently Editor-at-large of *The European Journal of Control*

1 Introduction

Use of a Continuously Variable Transmission (CVT) in a car can reduce fuel consumption. Because engine revolutions can be chosen independently of vehicle speed, efficient operating points of the internal combustion engine can be used that are unreachable with a manual transmission or a stepped automatic transmission. Unfortunately, because the energy consumption of the CVT itself is higher than that of a manual transmission, this efficiency improvement is partly lost.

One sheave of each pulley of a pushbelt or chain type CVT is actuated axially to adjust the transmission ratio and to apply a belt clamping force. In conventional CVTs, this is done hydraulically. The CVT transmission ratio, which depends on the ratio of the primary and secondary clamping force, is controlled by the pressure in the cylinders.

However, hydraulic losses are substantial. The oil pump is directly coupled to the crankshaft of the ICE. To realise high shifting speeds at low engine speeds, for instance during an emergency stop or a kickdown, a large pump displacement is required. However, when the CVT ratio is held constant at higher engine speeds, for instance while cruising on a highway, an unnecessarily large oil flow from high pressure to sump leads to large energy losses. In Bonsen et al. (2005) and van Drogen and van der Laan (2004) it is shown that it is possible to reduce these actuation losses by means of controlling the slip in the variator. Using a slip control strategy the clamping forces are reduced to minimal values, directly reducing the power losses of the hydraulic system. Efficiency gains of up to 10% can be reached compared to conventional control strategies. Bradley and Frank (2002) present an alternative hydraulic system with servo-pumps for ratio and clamping force control. This system achieves approximately 5% fuel consumption reduction compared to a conventional hydraulic system. Also Faust et al. (2002) show that it is possible to achieve significant fuel reduction based on an optimised hydraulic system.

A major disadvantage of hydraulic actuation systems is that the compressibility of the oil increases with decreasing pressure. As a consequence, the required bandwidth for both ratio and clamping force control cannot be realised. Especially, slip control at low pressures requires a stiff actuation system to prevent the variator from excessive slip.

Yuki et al. (1995) developed an electromechanical actuation system to reduce the actuation losses. This system has the disadvantage that the clamping force is supported by a thrust bearing between the rotating shaft and the transmission housing, which leads to large power losses in these bearings. This limits the use of this system to low power applications, with low clamping forces.

van de Meerakker et al. (2004) propose an alternative electromechanical actuation system, called the Empact CVT. It uses a double epicyclic gear at each shaft with thrust bearings between the two sun gears to support the clamping force. The speed of these sun gears only differ during the ratio changes. In this way, the power losses in the thrust bearings are reduced significantly and the clamping device can be used for high power applications. Because of the high stiffness of the actuation system, even at low clamping forces, the Empact CVT is very suitable for slip control.

For design evaluation and control design, the dynamics of the Empact actuation system are thoroughly investigated. This paper presents a simulation model of the Empact CVT, which incorporates these dynamics. This model is used for system performance evaluation, control design and testing and evaluation of the closed-loop system. Apart from the dynamics of the actuation system, also the physical properties of the variator, like slip dynamics, are incorporated.

Section 2 first gives a description of the Empact CVT and the test environment. Section 3 focuses on the dynamical behaviour of the Empact CVT. A lumped parameter model will be introduced. It will be shown that the clamping force ratio and traction curve of the variator have significant influence on the dynamics. A non-linear variator model is needed for a sufficiently accurate description of the variator dynamics. Section 4 discusses the formulation of this model. Section 5 shows some further implementation issues of the simulation model, like friction models and closed-loop control. Finally, in Section 5.2 simulation results are validated using measurement results from a prototype transmission.

2 The Empact CVT

Figure 1 shows a concept drawing of the Empact CVT, whereas Figure 2 shows a more schematic representation. At the primary or input shaft, one of the ring gears of the double epicyclic set is fixed to the transmission housing. The other ring gear is actuated using a servomotor, the primary servo M_p. This servo is connected by a worm to the worm gear on the ratio adjustment ring. At the secondary shaft, one ring gear is directly in mesh with the primary actuated ring gear. The secondary clamping force adjustment ring gear is connected to a second servomotor M_s using a chain gear and a planetary reduction. Important characteristic of the epicyclic sets is that the carriers at each shaft are combined and the dimensions of all epicyclic sets are equal. By rotating the primary servo M_p, a relative rotation between the two sun gears of the epicyclic sets at both shafts is realised. A planetary roller spindle translates this rotation into a translation of the moveable pulley sheaves, resulting is a CVT ratio change. The secondary servo M_s is used for two tasks. Firstly, when changing the ratio in a CVT, the displacements of the moveable sheaves of the primary and secondary pulley are not exactly equal. The secondary servo can compensate for this difference. Secondly, by adjusting the torque delivered by the secondary servo, the clamping forces and hence the slip in the variator can be controlled.

The primary actuator M_p of the Empact is a brushed DC servo, which operates at 48 [V]. It is able to deliver a continuous torque of 3.5 [Nm]. The secondary actuator M_s is a brushless type DC servo, also operating at 48 [V]. It can deliver a continuous torque of 0.6 [Nm]. Due to the planetary reduction gear of 1:16, the chain reduction of 1:4 and the spindles with 4 [mm/rev] pitch, a maximum constant clamping force of approximately 30 [kN] can be realised.

Figure 2 shows a schematic representation of the set-up for experiments with the Empact CVT. This set-up consists of a driving motor, a torque converter, the Empact CVT including

Figure 1 Concept drawing of the Empact CVT

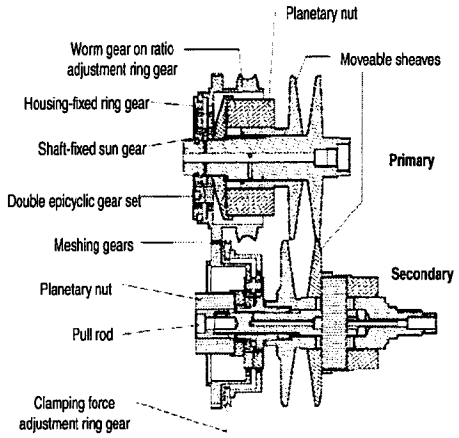

Figure 2 Schematic representation of empact model

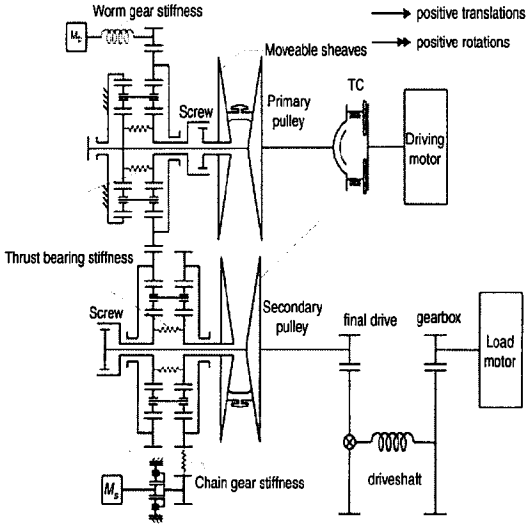

final drive reduction, a fixed gear reduction and a load motor. The CVT is connected to the fixed gear reduction by a single driveshaft. The motors can deliver a maximum torque of 267 [Nm], have a maximum speed of 525 [rad/s] and can deliver up to 81 [kW]. The fixed gear reduction is used to match the load motor characteristics to the driving motor characteristics. The output of the CVT is connected to the fixed gear reduction by a single driveshaft. The differential gear is locked, so all power can be directed to the driveshaft.

In the experimental set-up, the primary and secondary actuator rotation, θ_{mp} and θ_{ms}, respectively, the rotation of the driving (θ_d) and load (θ_l) motor and the primary and secondary shaft speed ω_p and ω_s, respectively, are measured. Furthermore, the torques at the input shaft, driveshaft and the torque between the fixed gear reduction and load motor are measured. The torques of the primary and secondary actuator, T_{mp} and T_{ms}, are considered to be known, based on the characteristics of the servo motors and servo amplifiers.

3 Dynamical analysis

During the experiments, the torque converter is used in lock-up mode only. In this case, it can be modelled as a torsion

spring. The driveshaft is modelled as a rotational spring element. The worm and bearing stiffness of the primary actuation are represented as a torsion spring between the primary servo and the worm. The chain at the secondary actuation is also modelled as a longitudinally flexible element (Müller, 2000). Furthermore, the thrust bearings between the sun gears at the primary and at the secondary side are modelled as linear springs. Pulley bending is accounted for by means of a torsion spring element. Finally, the pushbelt is represented as a flexible element. The stiffness of this element is a combination of the longitudinal stiffness of the steel bands of the pushbelt and the stiffness of the pushing segments on the tense side. All other elements, that is, the spindles and the gears, of the Empact CVT are considered rigid in the frequency range of interest (below 200 [Hz]).

All flexible elements are subjected to damping. Other non-conservative forces that act on the system are viscous friction acting on the bodies and a damping force in the variator according to Shafai's model (Shafai et al., 1995).

To describe the dynamics of the Empact, the Lagrangian approach is used. Before describing the kinematic relations in the Emact actuation system, the notation of the position variables of the bodies is introduced. The rotation of the gears of the epicyclic sets are referred to as $\theta_{\alpha\beta\gamma}$. Here, $\alpha = \{a, c, p, s\}$ refers to the annulus, carrier, planet and sun, respectively, $\beta = \{l, r\}$ refers to the left and right epicyclic set and $\gamma = \{p, s\}$ refers to the primary or secondary side of the Empact CVT, respectively. Furthermore, the translation of the moveable pulley sheaves, the rotation of the CVT shafts, the rotation of the servomotors, the translation of the nut of both spindles and the bending of the pulleys will be referred to as x_γ, θ_γ, $\theta_{m\gamma}$, $x_{n\gamma}$ and $\theta_{b\gamma}$, respectively. Finally, the rotations of the driving and load motor are referred to as θ_d and θ_l. Sign conventions for translations and rotations are shown in Figure 2.

3.1 Kinematics

The basis of the Empact system are the double epicyclic sets at both shafts. The kinematic relations of a single epicyclic gear are given by

$$\omega_{\text{sun}} = (z+1)\omega_{\text{carrier}} - z\omega_{\text{annulus}}$$

$$\omega_{\text{sun}} = z\omega_{\text{annulus}} - (z-1)\omega_{\text{planet}}$$

where ω_{sun}, ω_{carrier}, ω_{annulus} and ω_{planet} are the angular velocities of the sun, carrier, annulus and planet gears, respectively and z is the ratio of the radii of the annulus and of the sun gear. Extending these relations to the epicyclic sets of the Empact system results in

$$(z+1)\,\dot{\theta}_{clp} = \dot{\theta}_p \tag{1}$$

$$\dot{\theta}_{srp} = \dot{\theta}_p - z\dot{\theta}_{arp} \tag{2}$$

$$(z-1)\,\dot{\theta}_{plp} = -\dot{\theta}_p \tag{3}$$

$$(z-1)\,\dot{\theta}_{prp} = -\dot{\theta}_p + 2z\dot{\theta}_{arp} \tag{4}$$

$$(z+1)\,\dot{\theta}_{cls} = \dot{\theta}_s + z\dot{\theta}_{ars} \tag{5}$$

$$\dot{\theta}_{sls} = z\dot{\theta}_{arp} + \dot{\theta}_s + z\dot{\theta}_{ars} \tag{6}$$

$$(z-1)\,\dot{\theta}_{pls} = -2z\dot{\theta}_{arp} - \dot{\theta}_s - z\dot{\theta}_{ars} \tag{7}$$

$$(z-1)\,\dot{\theta}_{prs} = -\dot{\theta}_s + z\dot{\theta}_{ars} \tag{8}$$

In these relations, the fact that one primary annulus is fixed to the ground and the other primary annulus is connected to one secondary annulus, is taken into account. The translation from the sun rotations to the pulley translation is performed by the spindles at both shafts. The kinematic relation of a spindle is given by

$$\dot{x}_b - \dot{x}_n = s\left(\dot{\theta}_b - \dot{\theta}_n\right)$$

where s is the pitch of the spindle, $\dot{x}_b$ and $\dot{x}_n$ are the translational velocities of the spindle bold and nut, whereas θ_b and θ_n are the rotations of these bold and nut. For the primary spindle with pitch s and the secondary spindle with opposite pitch $(-s)$, this relation results in

$$\dot{x}_{np} = \dot{x}_p - s\left(\dot{\theta}_{srp} - \dot{\theta}_p\right) = sz\dot{\theta}_{arp} + \dot{x}_p \tag{9}$$

$$\dot{x}_{ns} = \dot{x}_s + s\left(\dot{\theta}_{sls} - \dot{\theta}_s\right) = sz\dot{\theta}_{arp} + sz\dot{\theta}_{ars} + \dot{x}_s \tag{10}$$

With these kinematic relations, the system can be described by 12 degrees of freedom, the entries of a vector $\underline{q}$:

$$\underline{q} = \left[\theta_p \;\; \theta_{mp} \;\; \theta_{arp} \;\; x_p \;\; \theta_s \;\; \theta_{ms} \;\; \theta_{ars} \;\; x_s \;\; \theta_d \;\; \theta_l \;\; \theta_{bp} \;\; \theta_{bs}\right]^T$$

The origin of these coordinates is defined as the position for all elements where the springs are not elongated at a certain geometric CVT ratio $r_{g0} = R_{p0}/R_{s0}$, where R_{p0} and R_{s0} are the nominal primary, respectively secondary running radius of the belt. For the geometric relation in the variator now holds:

$$L = 2a\cos(\varphi) + (\pi + 2\varphi)R_p + (\pi - 2\varphi)R_s \tag{11}$$

where L is the length of the pushbelt, a is the distance between the primary and secondary shaft, $\varphi = \arcsin\left(R_p - R_s/a\right)$ and

$$R_p = R_0 + \frac{1}{2\tan(\beta)}\left(x_p + \theta_{bp}R_{p0}\right)$$

$$R_s = R_0 + \frac{1}{2\tan(\beta)}\left(x_s + \theta_{bs}R_{s0}\right)$$

where β is the pulley wedge angle and R_0 is the running radius at $r_g = 1$. The nominal belt length is $L_0 = 2a + 2\pi R_0$ and hence the belt elongation is given by

$$\Delta L = L - L_0 \tag{12}$$

3.2 Lagrangian dynamics

The velocity of all components of the system in Figure 2 is completely determined by the generalised coordinates. Hence, the summation of the individual contributions of the components results in a quadratic relation for the total kinetic energy T,

$$T = \frac{1}{2}\dot{\underline{q}}^T M \dot{\underline{q}} \tag{13}$$

where M is the symmetric, positive, constant and non-diagonal mass matrix.

The total elastic energy V consists of the contributions of the spring between the primary servo M_p and the primary

epicyclic set, the spring between the secondary servo M_s and the secondary epicyclic set which models the chain reduction, the spring that accounts for the elasticity of the pushbelt, the springs that represent the thrust bearings in the epicyclic sets, the springs to model the pulley bending, the torque converter spring and the spring between the CVT and the fixed gear reduction. The final result for V is given by

$$V = \frac{1}{2}\underline{q}^T K \underline{q} \tag{14}$$

where K is the symmetric, semi-positive stiffness matrix. The elastic energy in the pushbelt weakly depends on the CVT-ratio, due to the belt elongation. If this dependency is neglected then K is a constant matrix.

The total power loss in the system is divided in a contribution L_v of the variator and a contribution L_a of the rest of the system. It is assumed that L_a is due to viscous friction in the spindle transmissions between the pulleys and the epicyclic sets, in the bearings and between the gears. Hence, L_a is given by

$$L_a = \underline{\dot{q}}^T \underline{F}_a; \quad \underline{F}_a = D_a \underline{\dot{q}} \tag{15}$$

where $\underline{F}_a$ is a vector of generalised loss forces, whereas D_a is a symmetric, semi-positive damping matrix.

The power loss in the variator L_v is due to the coupling between the rotation of the primary and secondary shaft. This coupling is realised by the transmitted belt torque at the secondary pulley T_s and the primary pulley T_p (Klaassen et al., 2004a), given by

$$T_s = \frac{2\mu\left(\nu, r_g\right) F_s R_s}{\cos(\beta)} \tag{16}$$

$$T_p = r_g T_s \tag{17}$$

where $r_g = R_p/R_s$ is the geometric CVT ratio, $\mu(\nu, r_g)$ is a slip and ratio dependent traction coefficient and F_s is the clamping force at the secondary pulley. Here, the torque loss in the variator is neglected. The slip ν in the variator is defined as

$$\nu = 1 - \frac{\omega_s}{\omega_p} r_g^{-1} \tag{18}$$

If the primary and secondary servos keep the CVT ratio and the clamping force constant, the belt torque $T_s = T_{s0} + \tilde{T}_s$ can be linearised at the constant geometric ratio r_{g0} and a nominal clamping force F_{s0}, resulting in

$$\tilde{T}_s = c_{br}\left(\frac{\omega_{s0}}{\omega_{p0}}\tilde{\omega}_p - \tilde{\omega}_s\right); \qquad c_{br} = \frac{2\mu'\left(\nu_0, r_{g0}\right) F_{s0} R_{p0}}{\omega_{p0}\cos(\beta) r_{g0}} \tag{19}$$

where $\mu'(\nu_0, r_{g0})$ is the slope of the traction curve at the corresponding slip value. F_{s0} results from the nominal slip value ν_0 and constant ratio r_{g0} for a chosen T_{s0}. Hence, the belt torque can be modelled as a damper with damping constant c_{br} between the primary and secondary pulley. This can be described by the non-conservative energy function

$$Q = \frac{1}{2} c_{br}\left(\frac{\omega_{s0}}{\omega_{p0}}\tilde{\omega}_p - \tilde{\omega}_s\right)^2 \tag{20}$$

The power loss L_v in the variator is now defined by

$$L_v = \underline{\dot{q}}^T \underline{F}_v; \qquad \underline{F}_v = D_v \underline{\dot{q}} \tag{21}$$

where $\underline{F}_v$ is the vector of loss forces and the symmetric damping matrix D_v is given by

$$D_v = \frac{\partial}{\partial \underline{\dot{q}}}\left(\frac{\partial Q}{\partial \underline{\dot{q}}}\right)^T \tag{22}$$

Because the slope of the traction curve μ' is not positive in all operating points, this damping matrix is not semi-positive, but can also be negative.

The resulting equation of motion which describes the complete system, is now given by

$$M\underline{\ddot{q}} + D_a\underline{\dot{q}} + D_v\underline{\dot{q}} + K\underline{q} = \underline{f} \tag{23}$$

where the force vector $\underline{f}$ consists of the primary and secondary servo motor torques T_{mp} and T_{ms}, the driving and load motor torques T_d and T_l and the belt torques at the primary and secondary pulley T_s and T_p.

3.3 *Undamped eigenmodes*

Using the mass matrix M and the stiffness matrix K, the undamped eigenfrequencies f_r and corresponding eigenvectors can be calculated. Due to the fact that in the calculation of the undamped eigenmodes no power dissipation is present, there is no coupling between the primary and secondary shaft. In this case, three rigid body modes are present, that is, a rotation of the primary shaft, a rotation of the secondary shaft and a rigid body mode of the actuation system where the primary servo moves both pulleys. Furthermore, five low frequency ($f_r < 100$ [Hz]) and four high frequency modes are present. To get an impression of these mode shapes, Figure 3 shows the normalised potential energy of the nine elastic elements in each of the first five modes. The sign of the energy shows whether the corresponding spring is elongated or shortened.

Figure 3 Normalised potential energy of spring elements at $r_g o = 1$

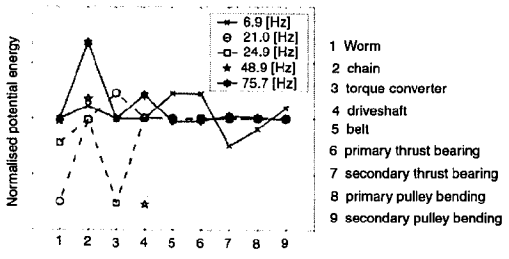

The lowest eigenfrequency of $f_r = 6.9$ [Hz] originates from the deformation of the chain transmission in the secondary

actuation, in combination with the deformation of thrust bearings and the belt and with the bending of the pulleys. The bearings, belt and pulleys themselves are fairly stiff, but due to the large reductions in the system, they greatly contribute to the flexibility. The second eigenfrequency at $f_r = 21.0$ [Hz] originates mainly from the flexibility of the worm transmission at the primary actuator. This mode is also influenced by the torque converter stiffness. The third mode at $f_r = 24.9$ [Hz] is the rotating mode of driving motor, torque converter stiffness and primary shaft. The fourth resonance at $f_r = 48.9$ [Hz] is the rotating mode of the secondary shaft, driveshaft and load motor. These two modes are decoupled, because the coupling by the belt is neglected in the undamped case. Note that the primary and secondary inertias are different from a vehicle, hence also the resonance frequencies are different. The last low frequency mode at $f_r = 75.7$ [Hz] originates from the deformation of the chain in the secondary actuation. The four high frequency eigenmodes all result from the translating parts of the actuation system. These modes are beyond the frequency range of interest and are left out of consideration in the remainder of this paper.

3.4 *Belt coupling*

The undamped eigenmodes correspond to the situation where the damping of the belt, described in Equations (16)–(20), is neglected. In this situation, with $c_{b_r} = 0$, the primary and secondary shaft are decoupled. If c_{b_r} is increased, a coupling between both shafts arises. This damping constant is determined by the derivative of the traction coefficient μ with respect to the slip ν. Figure 4 shows measurements results of μ in at $\omega_p = 225$ [rad/s] for three different CVT ratios (Bonsen et al., 2003). It can be seen that with increasing slip ν, the traction μ increases until a certain maximum value is reached. For higher slip values μ shows a decrease for $r_g = 1.1$ and $r_g = 2.26$, resulting in a negative damping coefficient c_{b_r}.

Figure 4 Traction curve in $r_g = 0.4$ (LOW), $r_g = 1.1$ (MED) and $r_g = 2.26$ (OD)

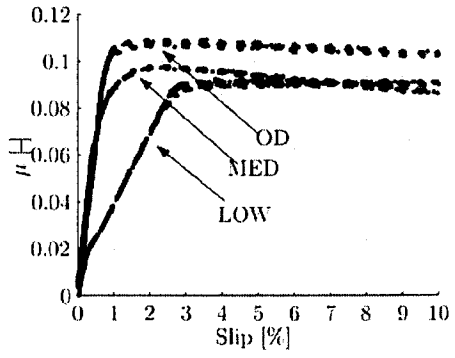

Figure 5 shows the root locus of the low frequency poles of the system (including damping now) for decreasing slip, from 4% to 0% at $r_{g0} = 1$, $\omega_{p0} = 100$ [rad/s] and a nominal belt torque of $T_{s0} = 200$ [Nm]. The damping coefficient c_{b_r} increases from small negative values for $\nu = 4\%$ to positive values. For negative c_{b_r}, some of the poles are located in the RHP, indicating unstable behaviour. It can be seen that the damping of the complex pole pair at 48.9 [Hz] increases as it turns back towards the real axis. At the real axis, one of these poles goes to $-\infty$, whereas the other tends towards the imaginary axis. Due to increasing coupling between the primary and secondary shaft, one of the rigid body mode poles moves from 0 towards negative real values. At approximately 11 [Hz], these two real poles become one complex pair. A further increase of the damping makes this pole pair turns towards the imaginary axis. The primary and secondary shaft are fully coupled in this case. From the two rigid body modes of the driveline, only one remains. The mode of the primary shaft is also influenced by the belt coupling and shifts from 24.9 [Hz] to 32.7 [Hz]. The modes at 6.0 [Hz] and at 21.0 [Hz] hardly are influenced by the belt coupling. The resonance from the secondary actuator and chain stiffness shifts from 75.7 [Hz] to 68.9 [Hz].

Figure 5 Root locus of poles for $\nu = 4\%$ at $r_{go} = 1$ (see online version for colours)

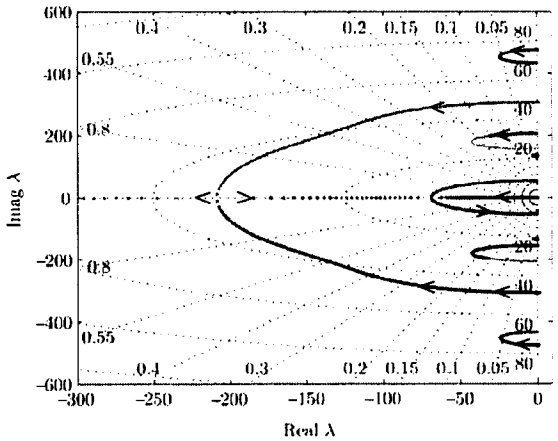

4 Variator model

The ADAMS simulation model by Kanokogi and Hoshino (2000) tries to capture the variator behaviour by modelling each component of the metal V-belt as a rigid or flexible body. To analyse the belt-pulley-contact they use contact elements. They claim to obtain results similar to physical tests. However, the CPU time for a simulation time if very large due to the large of degrees of freedom. This model is suitable for variator analysis, but not for driveline simulations where complete driving cycles must be run. A model for driveline simulations has to be computationally fast, but nevertheless has to incorporate physical phenomena like slip in the variator, clamping force ratio and shifting losses. Whereas slip in the variator and shifting losses are incorporated in the model described in the previous section, in this section a model is presented, which provides an estimation for the clamping forces in the variator. In the model the clamping force at the primary and secondary pulley, F_p and F_s, respectively, are not prescribed, but result from other quantities in the system (Klaassen et al., 2004b).

A similar approach for a chain drive CVT is presented by Lebrecht et al. (2005).

4.1 Clamping force estimation

The clamping forces between the belt and pulleys are calculated using a model based on Coulomb friction. This model is thoroughly described in Vroemen (2001) and Kobayashi et al. (1998). In Commissaris (2005) it is shown that the clamping force ratio, according to this model, fairly well agree with experimentally determined clamping force ratio.

The model gives insight in the tensile force S in the bands of the belt and compressive forces Q between the blocks of the belt. Four different regimes of operation have to be distinguished. Firstly, a distinction is made between underdrive (U) and overdrive (O), defined by $r_g \leq 1$ and $r_g > 1$, respectively. Secondly, a distinction is made between a driving (D) situation and a driven or reversed situation (R). Basically, in the driving situation, defined by $(S_1 - S_0)R_p \leq T_p$, the primary shaft drives the secondary shaft. In the reversed situation, defined by $(S_1 - S_0)R_p > T_p$, the secondary shaft drives the primary shaft. In these expressions, T_p is the input torque at the primary pulley, S_0 the minimum and S_1 the maximum tension force in the belt. Figure 6 shows the Underdrive Driving (UD) case. For this regime, the compression force Q is built up at the primary pulley along the active compression arc φ_1, leaving an idle compression arc $\varphi_p - \varphi_1$ where $Q = 0$. The tension force S is reduced from S_1 to S_0 over the complete arc φ_p. At the secondary pulley, Q is reduced over the active arc φ_2. S is here built up over the same arc as it is reduced at the primary pulley, namely φ_p. At this driven pulley both an idle compression arc, where $Q = Q_0$, and an idle tension arc, where $S = S_0$, exist. For the other regimes, the same active and idle arcs exist, only defined in a different way. For the sake of shortness, only the UD regime will be discussed here. Other regimes can be described in similar ways.

Figure 6 Tension and compression forces for $r_g \leq 1$ and $(S_1 - S_0)R_p \leq T_p$ (UD)

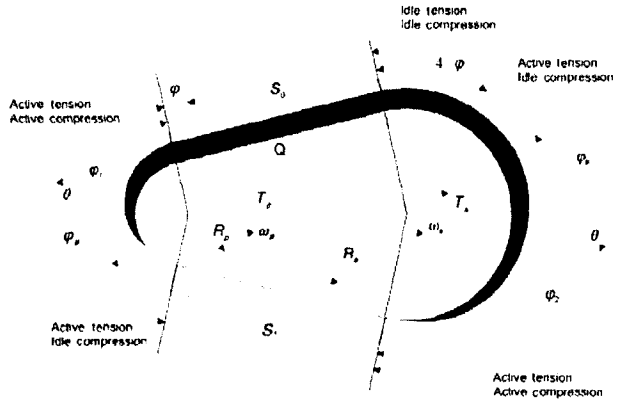

Vroemen (2001) describes an approach to calculate the primary clamping force F_p, given the input torque T_p, the speed ratio $r = \omega_s/\omega_p$ and the secondary clamping force F_s. The lowest of the tension forces S_0 S_1 is calculated using an iterative procedure. Once this value is known, it is straightforward to calculate the active compression arcs φ_1 and φ_2 and the primary clamping force F_p. This method is, however, not suitable to use in the simulation model described in this paper, because here the secondary clamping force is not known a priori. Furthermore, the iterative procedure preferably should be avoided, because this increases the calculation time.

To get an expression for both the primary and secondary clamping force, a different formulation is used. Summarised, in this approach first an explicit expression is obtained for the tension force S in the belt, based on the elongation of the belt. From this expression, the compression force Q can be obtained. Next, the active arcs are estimated using the maximum compression force Q_0. It is then straightforward to calculate the clamping forces F_p and F_s. This approach, described in more detail below, is, amongst others, based on the assumption that spiral running can be neglected.

4.1.1 Tension force

The tension forces in the belt cause it to elongate. This elongation can be expressed as

$$\Delta L = \frac{1}{EA}\int_y S(y)\mathrm{d}y \tag{24}$$

where y is a longitudinal coordinate along the belt, E is Young's modulus and A is the cross sectional area of the bands. Rewriting this equation for the UD case gives

$$\begin{aligned}\Delta L E A = &\int_{-1/2\varphi_p}^{1/2\varphi_p} S^p(\theta)R_p d\theta + \int_{1/2\varphi_s-\varphi_p}^{1/2\varphi_s} S^s(\theta)R_s d\theta + \ldots \\ &(S_0 + S_1)a\cos(\varphi) + S_0 R_s 4\varphi\end{aligned} \tag{25}$$

Here $S^p(\theta)$ and $S^s(\theta)$ are the tension forces along the primary, respectively the secondary active tension arcs (see Figure 6), expressed as

$$S^{p,s}(\theta) = K_S^{p,s} e^{-\mu_1 s_1 \theta} + F_B \tag{26}$$

where μ_1 is the friction coefficient between the bands and the elements, F_B is the centrifugal force of the bands and $s_1 = 1$ for $r_g < 1$ at the primary side and $s_1 = -1$ at the secondary side, where the integration constants $K_S^{p,s}$ are defined as

$$K_S^p = (S_0 - F_B)e^{\mu_1 \varphi_p/2}$$
$$K_S^s = (S_0 - F_B)e^{-\mu_1(\varphi_s/2-\varphi_p)}$$

Furthermore, by using the relation

$$S_1 = (S_0 - F_B)e^{\mu_1\varphi_p} + F_B \tag{27}$$

an explicit expression for S_0 can be obtained based on the elongation ΔL of the belt.

Using geometric properties of the variator, the elongation of the belt can also be calculated using the positions of the primary pulley x_p and secondary pulley x_s, according to $\Delta L = L - L_0$ (Equation (12)).

Now, by combining the Equations (24) and (12), an expression for the minimum tension force in the belt can be obtained as a function of the primary and secondary pulley positions.

4.1.2 Compression force

The next step on the path from pulley position to the clamping forces, is to calculate the compression force Q in the belt. The compression force at active compression arcs (Figure 6) can be expressed as

$$Q^{p,s}(\theta) = K_S^{p,s} e^{-\mu_1 s_1 \theta} + K_Q^{p,s} e^{-(\mu_2 s_2/\sin(\beta)\theta)) - Fc} \quad (28)$$

where the index p refers to the primary pulley and index s refers to the secondary pulley, $\mu_2 = \max(\mu)$ is the friction coefficient between the elements and the pulley, F_C is the centrifugal force of the elements, $s_2 = 1$ at the primary side and $s_2 = -1$ at the secondary side, whereas the integration constants $K_Q^{p,s}$ follow from Equation (28) with the boundary condition $Q^p(\theta) = 0$ for $\theta = (\varphi_p/2) - \varphi_1$ and $Q^s(\theta) = 0$ for $\theta = (\varphi_s/2)$, yielding

$$K_Q^p = \left(F_C - K_S^p e^{-\mu_1(\varphi_p/2-\varphi_1)}\right) e^{(\mu_2 s_2/sin(\beta))(\varphi_p/2-\varphi_1)}$$

$$K_Q^s = \left(F_C - K_S^s e^{-\mu_1(\varphi_s/2)}\right) e^{(\mu_2 s_2/sin(\beta))\varphi_s/2}$$

The maximum compression force $Q_0 = \max(Q)$ can be obtained from

$$T_p = Q_0 R_p + (S_1 - S_0)(R_p + \Delta R) \quad (29)$$

where ΔR is the distance between the radius of the bands R_p and that of the rocking edges of the V-belt segments.

4.1.3 Active compression arcs

By introducing the boundary condition for Q, for example $Q(\pi/2 - \varphi - \varphi_1) = 0$, an expression can be obtained for the maximum compression force Q_0 as a function of the active compression arcs. For the UD case these relations translate to

$$Q_0 = (S_0 - F_B)\left(1 - e^{(\mu_1 - (\mu_2/\sin(\beta)))\varphi_1}\right) + \cdots \quad F_C\left(e^{-(\mu_2/\sin(\beta))\varphi_1} - 1\right) \quad (30)$$

for the primary pulley and

$$Q_0 = (S_0 - F_B)\left(e^{\mu_1(\varphi_p - \varphi_2)} - e^{-(\mu_2/\sin(\beta))\varphi_2 + \mu_1\varphi_p}\right) + \cdots F_C\left(e^{-(\mu_2/\sin(\beta))\varphi_2} - 1\right) \quad (31)$$

for the secondary pulley. An explicit solution for φ_1 and φ_2 can not be found from these equations. However, if the exponential functions are approximated by a second order approximation, for example $e^{-\mu_1\varphi_2} = a + b\varphi_2/c + d\varphi_2$, it is possible to find an explicit solution. Figure 7 shows the estimation of φ_1 and the estimation error as a function of the tension force S_0 and the compression force Q_0 in the belt.

It can be seen that when a large tension force is present in comparison to the compression force, the active arc is small, whereas the active arc increases to the complete wrapped angle when the compression force increases or the tension force decreases.

4.1.4 Clamping force

Now the tension force, compression force and active arcs are known, it is possible to find the primary clamping force F_p and secondary clamping force F_s by integrating the sum of the tension and compression force over the wrapped angles, φ_p and φ_s, respectively.

It must be noted that the integration constants $K_S^{p,s}$, $K_Q^{p,s}$, s_1 and s_2 and the expressions for S, Q, F_p and F_s depend on the regime of operation of the variator, described in the beginning of this section.

5 Simulation model

5.1 Complete non-linear dynamic model

In the resulting simulation model, the linearised belt coupling is replaced with the belt coupling described by Equation (16). To obtain an accurate estimation of the slip in the variator, the traction curves shown in Figure 4 are implemented in the simulation model.

The connection between the primary and secondary moving pulley sheaves, which was described by the belt elongation in Equation (12), is replaced by the non-linear variator model described in Section 4.

Furthermore, to be able to estimate the losses of the transmission, friction models are implemented for all bearings, spindles, gears and the variator. The details of these models are not discussed here, but it is mentioned that Lugre friction models (Olsson et al., 1998) are used to have a continuous representation of the friction. Besides the possibility to include hysteresis in this model, it also reduces the simulation times significantly compared to non-continuous friction models. The estimates for the friction levels are partly obtained from catalogue data and partly from measurements.

Figure 7 Estimation of φ_1 at $r_g = 1$ and $\omega_p = 250$ [rad/s] (see online version for colours)

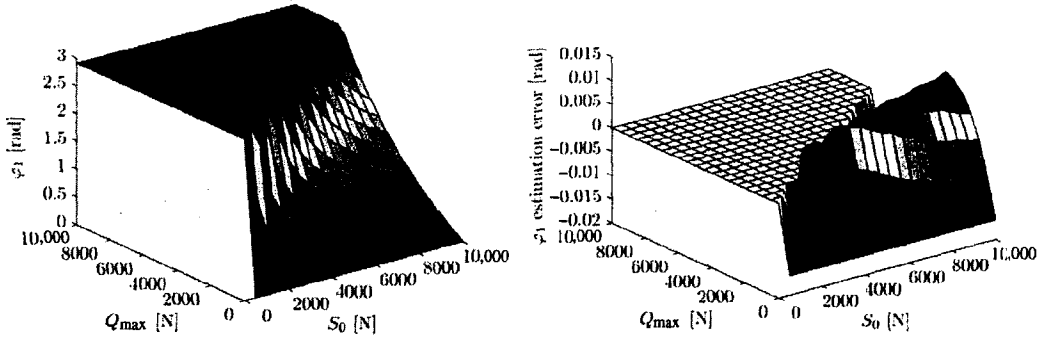

4.1.2 Compression force

The next step on the path from pulley position to the clamping forces, is to calculate the compression force Q in the belt. The compression force at active compression arcs (Figure 6) can be expressed as

$$Q^{p,s}(\theta) = K_S^{p,s} e^{-\mu_1 s_1 \theta} + K_Q^{p,s} e^{-(\mu_2 s_2/\sin(\beta)\theta))-F_C} \quad (28)$$

where the index p refers to the primary pulley and index s refers to the secondary pulley, $\mu_2 = \max(\mu)$ is the friction coefficient between the elements and the pulley, F_C is the centrifugal force of the elements, $s_2 = 1$ at the primary side and $s_2 = -1$ at the secondary side, whereas the integration constants $K_Q^{p,s}$ follow from Equation (28) with the boundary condition $Q^p(\theta) = 0$ for $\theta = (\varphi_p/2) - \varphi_1$ and $Q^s(\theta) = 0$ for $\theta = (\varphi_s/2)$, yielding

$$K_Q^p = \left(F_C - K_S^p e^{-\mu_1(\varphi_p/2-\varphi_1)}\right) e^{(\mu_2 s_2/sin(\beta))(\varphi_p/2-\varphi_1)}$$

$$K_Q^s = \left(F_C - K_S^s e^{-\mu_1(\varphi_s/2)}\right) e^{(\mu_2 s_2/sin(\beta))\varphi_s/2}$$

The maximum compression force $Q_0 = \max(Q)$ can be obtained from

$$T_p = Q_0 R_p + (S_1 - S_0)(R_p + \Delta R) \quad (29)$$

where ΔR is the distance between the radius of the bands R_p and that of the rocking edges of the V-belt segments.

4.1.3 Active compression arcs

By introducing the boundary condition for Q, for example $Q(\pi/2 - \varphi - \varphi_1) = 0$, an expression can be obtained for the maximum compression force Q_0 as a function of the active compression arcs. For the UD case these relations translate to

$$Q_0 = (S_0 - F_B)\left(1 - e^{(\mu_1 - (\mu_2/\sin(\beta)))\varphi_1}\right) + \cdots \\ F_C\left(e^{-(\mu_2/\sin(\beta))\varphi_1} - 1\right) \quad (30)$$

for the primary pulley and

$$Q_0 = (S_0 - F_B)\left(e^{\mu_1(\varphi_p - \varphi_2)} - e^{-(\mu_2/\sin(\beta))\varphi_2 + \mu_1\varphi_p}\right) \\ + \cdots F_C\left(e^{-(\mu_2/\sin(\beta))\varphi_2} - 1\right) \quad (31)$$

for the secondary pulley. An explicit solution for φ_1 and φ_2 can not be found from these equations. However, if the exponential functions are approximated by a second order approximation, for example $e^{-\mu_1\varphi_2} = a + b\varphi_2/c + d\varphi_2$, it is possible to find an explicit solution. Figure 7 shows the estimation of φ_1 and the estimation error as a function of the tension force S_0 and the compression force Q_0 in the belt.

It can be seen that when a large tension force is present in comparison to the compression force, the active arc is small, whereas the active arc increases to the complete wrapped angle when the compression force increases or the tension force decreases.

4.1.4 Clamping force

Now the tension force, compression force and active arcs are known, it is possible to find the primary clamping force F_p and secondary clamping force F_s by integrating the sum of the tension and compression force over the wrapped angles, φ_p and φ_s, respectively.

It must be noted that the integration constants $K_S^{p,s}$, $K_Q^{p,s}$, s_1 and s_2 and the expressions for S, Q, F_p and F_s depend on the regime of operation of the variator, described in the beginning of this section.

5 Simulation model

5.1 Complete non-linear dynamic model

In the resulting simulation model, the linearised belt coupling is replaced with the belt coupling described by Equation (16). To obtain an accurate estimation of the slip in the variator, the traction curves shown in Figure 4 are implemented in the simulation model.

The connection between the primary and secondary moving pulley sheaves, which was described by the belt elongation in Equation (12), is replaced by the non-linear variator model described in Section 4.

Furthermore, to be able to estimate the losses of the transmission, friction models are implemented for all bearings, spindles, gears and the variator. The details of these models are not discussed here, but it is mentioned that Lugre friction models (Olsson et al., 1998) are used to have a continuous representation of the friction. Besides the possibility to include hysteresis in this model, it also reduces the simulation times significantly compared to non-continuous friction models. The estimates for the friction levels are partly obtained from catalogue data and partly from measurements.

Figure 7 Estimation of φ_1 at $r_g = 1$ and $\omega_p = 250$ [rad/s] (see online version for colours)

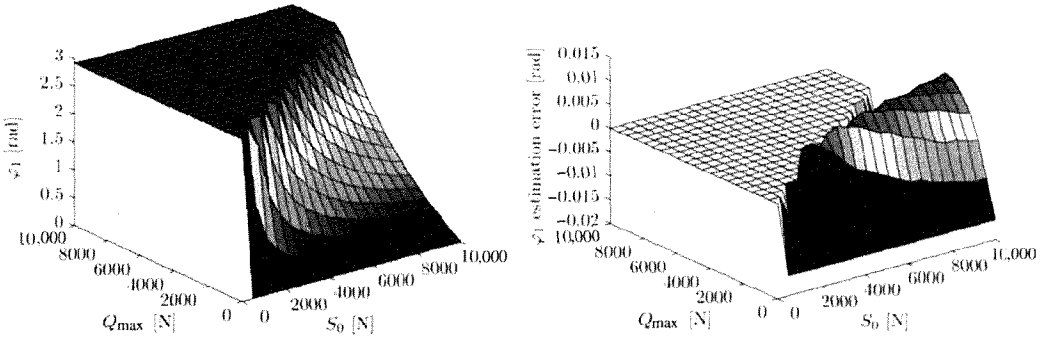

The control set-up, including parameters, are identical in simulation and measurement. The design of the controllers is beyond the scope of this paper, however the type of controllers is mentioned here. To control the ratio, a PID feedback on the position of the primary servo is used. The actuator position reference is calculated from the ratio reference using the geometric relations of the variator. In this experiment, the clamping force nor the slip in the variator are directly controlled. Instead, an open loop torque at the secondary actuator is used to set the clamping force in the system. Additional to this, a proportional feedback on the secondary actuator velocity is used. The reference speed is obtained from the ratio reference. This feedback has the advantage that a correction is made for the actuator movement, preventing the actuator from stick. Furthermore, a feedforward to compensate for the friction is used. Finally, the primary shaft velocity is controlled using a PI controller.

5.2 *Validation results*

Figure 8 shows a comparison of results from a simulation and measurement at the testrig. The pictured results start at a constant input speed of $w_p = 150$ [rad/s], load torque of $T_{\text{sec}} = 20$ [Nm] and secondary servo torque of $T_{\text{ms}} = 0.2$ [Nm], which corresponds to approximately $F_s = 10$ [kN] in stationary conditions. Firstly, the CVT shifts from $r_g = 0.5$ to $r_g = 2.0$ with $\dot{x}_p = 2$ [mm/s]. At that point, the secondary actuator torque is increased to $T_{\text{ms}} = 0.4$ [Nm]. Next, the load torque is increased to 90 [Nm]. Finally, the CVT shifts back to $r_g = 0.5$ and the load torque is increased to 200 [Nm].

To match the results of the simulation model to the results from the measurement, the friction plays a significant role. Especially, the Coulomb friction levels of the worm gear and spindles are high. During shifting of the variator, the friction in the spindles decreases the actual clamping forces in the variator. The hysteresis of the friction also has influence on the steady state clamping force, as can be seen from Figure 9(c). For instance, after the increase of the secondary actuator torque from 0.2 to 0.4 [Nm], the expected secondary clamping force would be 20 [kN]. However, due to the friction in the actuation system, the actual clamping force is only 18 [kN]. Another important effect of the friction is that it provides the hold torque for the primary servo when the variator is not shifting. This decreases the primary servo torque T_{mp} to approximately 0 [Nm]. Without the presence of friction, T_{mp} would be dependent on the clamping force ratio κ and only be zero when $\kappa = 1$. The simulation results show very good similarity to the measurement result. However, the slip in the measurement is significantly higher than the slip in the simulation. During shifting this can partly be explained by the fact that radial slip is not accounted for by the variator model. Due to slip in radial direction, the slip in tangential direction also increases. However, when the CVT is not shifting, the slip is also larger in the measurement than in the simulation. This could be due to a wrong estimation of the friction in the actuation system. This is however not likely, because the estimated primary servo torque T_{mp}, which depends mainly on the friction losses, shows very good similarity. A third cause could be that the traction coefficient μ of the Empact CVT differs significantly from the traction curves shown in Figure 4, which were measured on a different variator. However, a decrease by a factor of two seems very large and is not expected. Despite of the difference in the slip level, the dynamical behaviour of the slip shows good similarity to the measurement results.

Figure 8 Simulation results (dashed-line) and measurement results (solid line) (a) CVT ratio r_g, (b) slip ν, (c) primary servo torque T_{mp}, (d) secondary servo torque T_{ms}, (e) input torque and output torque and (f) primary and secondary shaft velocity

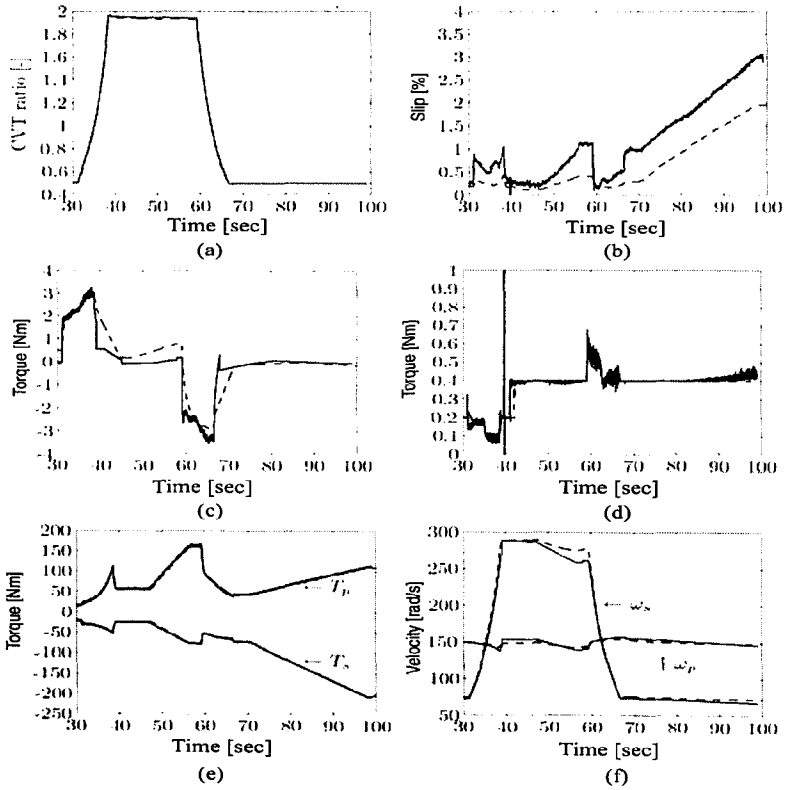

Figure 9 Additional simulation results (a) tension forces, (b) compression force, (c) clamping forces and (d) active arcs

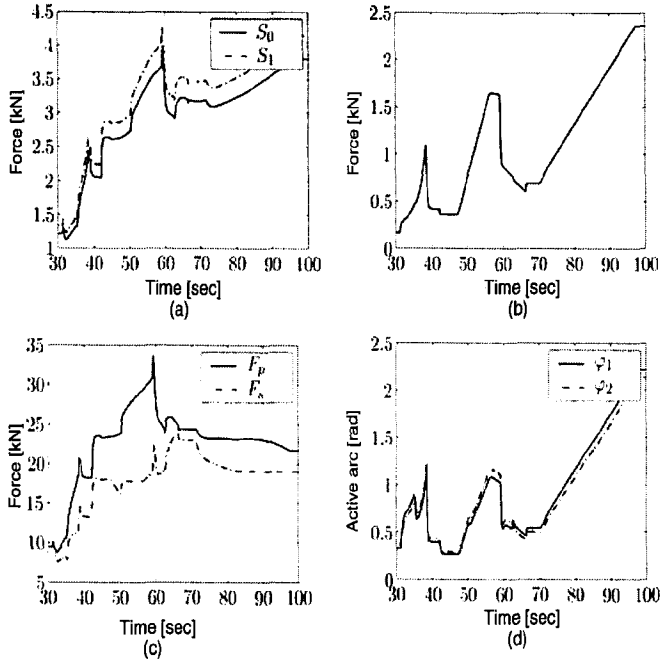

Also, due to this large friction in the system, the eigenmodes are largely suppressed. Figure 9 also shows the estimated tension and compression forces and the active compression arcs during the simulation.

6 Conclusions

The presented simulation model of the Empact CVT shows similar behaviour compared to a prototype of this transmission. The model is suitable to use for system evaluation, control design and testing of the resulting controlled system.

The dynamical analysis shows that, due to the large transmission ratios in the actuation system, the contribution of the bearings, belt and pulleys to the eigenmodes is significant. Although, the stiffness of these elements is fairly high, the resulting resonance frequencies are relatively low. Large control complications are not expected, but the resonance frequency at 6.9 [Hz] limits the possible performance of a slip controller. When linearised, the coupling of the primary and secondary pulley by the pushbelt can be modelled as a linear damper. The damping constant depends significantly on the slope of the traction coefficient in the variator. In practice, this slope varies from positive values to negative with increasing slip in the variator. As a result, the pole locations of the system depend significantly on the slope of the traction curve. At negative slope some of the poles are located in the RHP, indicating unstable behaviour. When using slip control, the reference slip level is near the maximum of the traction coefficient. The unstable behaviour in this area must be taken into account in the control design.

The presented simulation model combines the linear dynamics of the actuation system of the Empact CVT, with a non-linear description of the variator. The clamping forces in the variator are not prescribed, but result from physical quantities in the CVT. Based on the elongation of the bands of the belt, the clamping forces can be expressed explicitly. The rotational coupling of the primary and secondary shaft is described by a belt torque, which depends on the clamping forces, traction coefficient and CVT ratio. In this way, slip in the variator is incorporated. Furthermore, Lugre friction models are used to describe torque losses in the system.

The simulation results show very good similarity to results from measurement at a prototype transmission. The friction in the system plays a significant role in the dynamical behaviour. It decreases the actual clamping forces in the variator when the variator is shifting. Also, the steady state clamping forces are influenced by hysteresis of the friction. Although, the dynamics of the slip is well described, the slip value in the simulation model is smaller than in practice. This could be due to the used traction curves in the model, which are obtained from a different variator.

References

Bonsen, B., Klaassen, T., Pulles, R., Simons, S., Steinbuch, M. and Veenhuizen, P. (2005) 'Performance optimization of the push-belt cvt by variator slip control', *International Journal of Vehicle Design*, Vol. 39, pp.232–256.

Bonsen, B., Klaassen, T., van de Meerakker, K., Veenhuizen, P. and Steinbuch, M. (2003) 'Analysis of slip in a continuously variable transmission', *Proceedings of Imece*, No. 41360.

Bradley, T. and Frank, A. (2002) 'Servo-pump hydraulic control system performance and evaluation for cvt pressure and ratio control', *Proceedings of VDI CVT 2002 Congress*, (VDI-Berichte 1709), pp.35–41.

Commissaris, G.A. (2005) 'Validation of clamping force models using the power loop test rig', Master's Thesis, Technische Universiteit Eindhoven, DCT-2005.111.

Faust, H., Homm, M. and Reuschel, M. (2002) 'Efficiency-optimised cvt hydraulic and clamping system', *Proceedings of VDI CVT 2002 Congress*, number VDI-Berichte 1709, pp.43–58.

Kanokogi, K. and Hoshino, H. (2000) 'Simulation of metal pushing type v-belt for CVT', *Proceedings of the 15th ADAMS European User Conference.*

Klaassen, T., Bonsen, B., van de Meerakker, K., Steinbuch, M., Veenhuizen, P. and Veldpaus, F. (2004a) 'Nonlinear stabilization of slip in a continuously variable transmission', *Proceedings of CCA*, Taipei, Taiwan.

Klaassen, T., Vroemen, B., Bonsen, B., van de Meerakker, K., Steinbuch, M. and Veenhuizen, P. (2004b) 'Modelling and simulation of an electro-mechanically actuated pushbelt type continuously variable transmission', *Proceedings of IFAC Mechatronics*, No. 95, Sydney, Australia.

Kobayashi, D., Mabuchi, Y. and Katoh, Y. (1998) 'A study on the torque capacity of a metal pushing v-belt for CVTs', *SAE Technical Papers*, (980822).

Lebrecht, W., Ulbrich, H., Seckler, H. and Duhr, U. (2005) 'Transiente verstelldynamik von cvt-keilkettengetrieben', *Proceedings of Dynamik und Regelung von Automatischen Getrieben*, No. VDI-Berichte 1917, pp.247–268.

Müller, D.H. (2000) *Kettengetriebe*, BIK, Bremer Intitut für Konstruktionstechnick, Universität Bremen.

Olsson, H., Canudas de Wit, K. Å.C., Gäfvert, M. and Lischinsky, P. (1998) 'Friction models and friction compensation', *European Journal of Control*, Vol. 4, No. 3, pp.176–195.

Shafai, E., Simons, M., Neff, U. and Geering, H. (1995) 'Model of a continuously variable transmission', *Proceedings of the 1st IFAC Workshop on Advances in Automotive Control*, pp.99–107.

van de Meerakker, K., Rosielle, P., Bonsen, B., Klaassen, T. and Liebrand, N. (2004) 'Mechanism proposed for ratio and clamping force control in a CVT', *Proceedings of Fisita*, No. F2004F108.

van Drogen, M. and van der Laan, M. (2004) 'Determination of variator robustness under macroslip conditions for a pushbelt CVT', *Proceedings of SAE World Congress*, Detroit, USA.

Vroemen, B. (2001) 'Component control for the zero inertia powertrain', PhD Thesis, Eindhoven University of Technology.

Yuki, T., Takayama, M. and Kato, H. (1995) 'Development of dry hybrid belt CVT', *JSAE Review*, Vol. 16, pp.251–256.